Engineering with Computers
DOI 10.1007/s00366-016-0467-9

ORIGINAL ARTICLE

Hammerstein–Wiener based reduced-order model for vortex-induced non-linear fluid–structure interaction

Daniele Gallardo[1] · **Onkar Sahni**[1] · **Riccardo Bevilacqua**[2]

Received: 23 February 2016 / Accepted: 1 July 2016

Abstract Fluid–structure interaction (FSI) phenomena are of interest in several engineering fields. It is highly desirable to develop computationally efficient models to predict the dynamics of FSI. The complexity of modeling lies in the highly non-linear response of both the fluid and structure. The current study proposes an overall model containing two blocks corresponding to a force model and a structural model. The force model consists of two submodels: one for the amplitude and one for the frequency, where the latter is composed of an input/output linear model and a non-linear corrector. The amplitude submodel and the non-linear corrector term in the frequency submodel are modeled using an Hammerstein–Wiener modeling technique in which the non-linear input and output functions are determined by training neural networks using a training dataset. The current model is tested on a well-known fluid–structure interaction problem: a suspended rigid cylinder immersed in a flow at a low Reynolds number regime that exhibits a non-linear behavior. First, a training dataset is generated for a given input profile using a high-fidelity numerical simulation and it is used to train the reduced-order model. Subsequently, the trained model is given a different input profile (i.e., a validation profile) to compare its predictive capability against the high-fidelity numerical simulation. The validation profile is significantly different from the one used for training. The predictive performance of the current reduced-order model is further compared with the results obtained from a reduced-order model that uses polynomial fitting. We demonstrate that the current model provides a superior performance for the validation profile, i.e., it results in a better prediction.

Keywords Fluid-structure interaction · Vortex-induced vibration · Reduced-order modeling · Hammerstein-Wiener model · Neural network

List of symbols

A, B	Linear model's state space matrices
a_j^k	Predicted modal coefficient of the jth mode at time t_k
$\tilde{C}$	Map between the time evolution of dominant force frequency and $\tilde{\boldsymbol{V}}$, $\tilde{C} \in R^{1\times 2l}$
c	Structure damping coefficient (kg/s)
$d(t)$	Structural displacement at time t (m)
$\dot{d}(t)$	Structural velocity at time t (m/s)
$\ddot{d}(t)$	Structural acceleration at time t (m/s^2)
$\tilde{\boldsymbol{d}}$	Time history of the structural displacement (m)
$\tilde{d}_k$	Measured structural displacement at time t_k (m)
$\tilde{\boldsymbol{F}}$	Time history of the vertical force (N)
F_k	Modeled force at time t_k (N)
$\tilde{F}_k$	Measured force at time t_k (N)
F_{M_K}	Modeled force amplitude at time t_k (N)
$\tilde{\boldsymbol{F}}_u$	Upper envelope of $\tilde{\boldsymbol{F}}$ (N)
f_M	Function that relates F_{M_K} with u_k and t_k
$f_{w_{a_j}}$	HW model's input non-linear block for jth modal coefficient
f_{w_F}	HW model's input non-linear block for force amplitude

✉ Onkar Sahni
sahni@rpi.edu

Daniele Gallardo
Daniele.gallardo@yahoo.it

Riccardo Bevilacqua
bevilr@ufl.edu

[1] Department of Mechanical, Aerospace and Nuclear Engineering (MANE), Rensselaer Polytechnic Institute, 110 8th Street, Troy, NY 12180, USA

[2] Department of Mechanical and Aerospace Engineering, University of Florida, 939 Sweetwater Drive, Gainesville, FL 32608, USA

Published online: 20 July 2016

$f_{y_{a_j}}$	HW model's output non-linear block for jth modal coefficient
f_{y_F}	HW model's output non-linear block for force amplitude
$\hat{\text{fr}}_k$	Compensated (or corrected) dominant force frequency at time t_k (Hz)
g^j_{fr}	Function that relates a^k_j with u_k and time t_k
H_{a_j}	HW model's transfer function for jth modal coefficient
H_F	HW model's transfer function for force amplitude
K	Structure stiffness (N/m)
m	Structure mass (kg)
n_IN	Total number of neurons in the HW model's input non-linear block
n_{IN_MAX}	Maximum number of neurons possible in the HW model's input non-linear block
n_OUT	Total number of neurons in the HW model's output non-linear block
n_p	Total number of poles in the HW model's transfer function
n_PMAX	Maximum number of poles possible in the HW model's transfer function
n_z	Total number of zeroes in the HW model's transfer function
NRMSE_F	Normalized root mean square error in the modeled force amplitude
NRMSE_j	Normalized root mean square error in the modeled jth modal coefficient
o_j	jth zero of the HW model's transfer function
P	Number of POD modes used in reconstruction
p_j	jth pole of the HW model's transfer function
t	Time (s)
$\tilde{\boldsymbol{u}}$	Time history of the input velocity (m/s)
u_k	Input value at time t_k (m/s)
$\tilde{u}_k$	Measured input velocity at time t_k (m/s)
$\tilde{\boldsymbol{V}}$	Time history of the two-dimensional velocity vector field (m/s)
$\tilde{\boldsymbol{v}}_k$	Measured velocity vector field at time t_k (m/s)
$w_{\text{F}_{M_k}}$	Output of the HW model's input non-linear block for force amplitude
$w^k_{a_j}$	Output of the HW model's input non-linear block for jth modal coefficient
$\boldsymbol{x}_k$	State vector of the linear model at time t_k
$y^k_{a_j}$	Output of the HW model's transfer function for jth modal coefficient
$y_{\text{F}_{M_k}}$	Output of the HW model's transfer function for force amplitude
$\boldsymbol{z}_k$	State vector of the structural model
$\boldsymbol{\Phi}$	Map between the time evolution of the state vector $\boldsymbol{x}_k$ and $\tilde{\boldsymbol{V}}$, $\boldsymbol{\Phi} \in R^{2l\times r}$
$\boldsymbol{\psi}_j$	jth mode shape (POD)

1 Introduction

When an object is immersed in a moving fluid, a set of mutual interactions takes place in that the flow exerts a set of distributed forces on the object, while the object influences the surrounding flow because of its motion. These mutual interactions are referred to as fluid–structure interactions (FSI).

FSI phenomenon is present in a very broad range of engineering fields and manifests into a challenging factor due to its highly non-linear behavior. For example, in civil engineering it is important to consider wind-induced loading on tall buildings and bridges. An interesting recent study [1] casts a new light on one of the most infamous accidents involving FSI: the Tacoma Narrows Bridge.

When the FSI is not endangering the structural integrity of objects, it can still represent a serious problem. For example, in case of tall buildings, the interactions between the wind and building can generate significant displacement and acceleration that are experienced by the higher floor occupants [2, 3]. This can compromise the comfort level of the residents, making the higher floors unserviceable. Several studies have been carried out on the comfort level in tall buildings, and the works of Tamura et al. [4], Bashor et al. [5], and Kareem [6] are some examples. The non-serviceability of higher floors can have significant financial consequences, as demonstrated in the parametric study by Tse et al. [7]. For this reason, several studies have been conducted to improve the aerodynamic performance of tall buildings (i.e., by reducing the across-wind and along-wind acceleration). Some examples are the work of Kwok et al. [8], which analyzed the effect of edge configuration, and the extensive work of Kareem et al. [2], which investigated the effects of several passive and few active techniques. A recent work proposes the use of active flow control to improve the aerodynamic performance of tall buildings, see Menicovich et al. [9]. In this study, it is shown how the use of fluid-based aerodynamic modifications (FAMs) can significantly improve the aerodynamic performance, ultimately impacting the building costs.

In mechanical and aerospace engineering, FSI phenomena play an important role too. For example, FSI results in unsteady aerodynamic loading and blade vibrations, and dynamic stall under certain wind conditions. Furthermore, the effect of FSI on offshore wind turbines is also of interest (see [10]). Dynamic stall is an issue that affects helicopter blades too. A modeling work was conducted by Ham et al. [11, 12] and their findings were confirmed by studies conducted by McCroskey et al. [13] on a rotor model. These examples show that it is of significant importance to construct models and control strategies for FSI phenomena.

The first step is the construction of an efficient model that could be used in real-time applications, i.e., to predict the system dynamics given a certain set of input conditions. Specifically for FSI phenomena, such an efficient model must be capable of capturing the non-linear relationship between the incoming flow and the structural response.

A thorough review of existing modeling techniques for FSI problems has been done by Dowell and Hall [14]. As stated in this study, the range of models used for treating FSI varies significantly both in complexity and applicability. A possibility is to use the full-potential theory [15]. A common step to make the full-potential theory more treatable is by assuming the flow to be inviscid and irrotational [16]. By doing so, the flow equation can be solved using a non-linear wave equation for the velocity potential. This method presents significant complexity and requires numerical methods to solve the non-linear wave equation [16]. A further simplification assumes small body motions and a thin body profile. This approach has been extensively used to determine low-fidelity models that are commonly used in aeroelasticity for the so-called "flutter analysis" or "gust response analysis" [11, 12]. A step of increased complexity is taken in the time-linearized model (TLM), which assumes the flow solution to be non-uniform and dependent on the position [14]. TLMs are often solved using numerical methods; an example is the computation of a separated flow on a cascade of airfoils done by Florea et al. [17].

Using numerical methods, it is possible to employ much more complex non-linear dynamic models, including the full-potential theory without some of the simplifications discussed above. With numerical methods, it is indeed possible to study not only irrotational flow but also inviscid rotational flows and even viscous flows [14]. An example is the work of Tijdeman and Seebass [18], where transonic flow past an oscillating airfoil is analyzed, and further developments regarding the computation of unsteady transonic flow are described by Seebass et al. [19]. Further work regarding transonic flow has also been done by Nixon [20].

Recent work of Benaroya and Gabbai [21] introduced an interesting model for vortex-induced fluid–structure interactions which consists of a reduced-order model (ROM) composed of two coupled oscillators, one modeling the effects of the flow and the other modeling the structure. As it will become clear in the next section, the model formulated in this work borrows this idea.

ROM techniques represent an interesting and viable option to study FSI, as noted by Dowell and Hall [14]. Typically these techniques represent information regarding the flow in a finite set of modes, each one evolving with time. The superposition of these modes generates the observed global behavior. In the past, a number of ROM techniques have been devised, mainly to analyze the flow by decomposing the flow field in a set of modes that evolve in time. Studying these modes separately is easier, when compared to the whole flow field, and it is possible to get a more thorough understanding of the underlying phenomena.

The most commonly employed ROM technique consists of Karhunen–Loeve decomposition [22, 23] and is also known as proper orthogonal decomposition (POD) [24]. With this technique, the flow field information in a given time-span can be decomposed into a set of time-invariant modes. Each mode will then have an associated modal coefficient that is time dependent. By superimposing the modes, it is possible to reconstruct the flow field, i.e., at any given point in time and space. Moreover, it is possible to select only a subset of the total number of modes and determine an approximation of the flow field (e.g., using amount of energy captured as a criterion for modal selection or truncation). This feature is particularly interesting in modeling, because it helps to reduce the complexity or dimension of the system.

The POD technique has been widely used for studying FSI problems, mainly from a flow point of view, e.g., see [25, 26–28]. These studies include variations of the POD including, for example, double POD and filtered POD.

An alternative ROM technique is represented by the dynamic mode decomposition (DMD), e.g., see [29]. With this technique, every time-invariant mode is characterized by a specific frequency at which it pulsates in time. Moreover, every mode also accounts for temporal growth or decay. Chen et al. [30] have further devised an optimized method for DMD in computing an arbitrary number of modes from a specific dataset.

A common characteristic of all the above-mentioned ROM-related works is that they heavily concentrate on the flow analysis, not focusing on the structural aspects of the FSI problem. In contrast, work by Siegel et al. [31] used POD for both the structural and fluid dynamics from a closed-loop control point of view. In their work, a cylinder's 2D motion is prescribed by a controller that elaborates an actuation strategy based on the signal it gathers from sensors that detect the downstream flow conditions. However, the structure is used as an actuator to affect the flow rather than an element affected by the dynamics of the fluid.

Work by Gallardo et al. [32] demonstrated that it is possible to create a hybrid reduced-order model for FSI that incorporates the structural response. The model developed in their work captured the structural response of a rigid cylinder suspended in a flow at a low Reynolds number regime. This was done for a given input profile that was used in training the model and performance of the trained model was not tested on a different input profile (e.g., a validation profile). The model was made of two blocks,

one modeling the force exerted by the fluid on the structure and the other modeling the structural response. The force model was further divided into two submodels, one focusing on the force amplitude and the other on the force frequency. The submodel for frequency consisted of an input/output linear model and a non-linear corrector term. The structure of the frequency model is similar to the one developed by Ge and Wen [33] for the study of airflow in a contraction section. The non-linear corrector term compensates for the possibly non-linear behavior due to the surrounding flow (which is based on the flow field). It was based on POD modes to approximate the difference between the original data and output/response of the linear input/output model. Gallardo et al. [32] used a polynomial fitting within the non-linear corrector term to model the non-linear dynamics. However, the use of polynomial fitting limits the predictive performance of the hybrid ROM for different input profiles, which is a significant drawback.

To overcome this, the current study introduces a modeling technique that relies on a similar hybrid model structure explored by Gallardo et al. [32] but employs Hammerstein–Wiener (HW) architecture for model parameters. Specifically, for modeling the two significantly non-linear model components: force amplitude and the modal coefficients of the non-linear corrector term used in the frequency model. The HW model is composed of three blocks: a non-linear input block, an intermediate linear block and a non-linear output block [34]. Note that the HW architecture allows in distinguishing between the linear and non-linear blocks. This makes it modular and a suitable tool to analyze the relative influence of each non-linear block with respect to the linear block. For the non-linear blocks, we employ neural networks. This architecture is particularly suited for fluid–structure interaction applications because it has been developed to model highly non-linear phenomena. Some examples are the work of Zhu [34], Bai [35] and Bloemen et al. [36]. A thorough review of HW models using neural network-based non-linear blocks is described by Janczak [37].

The current model is tested on the same case study that was investigated by Gallardo et al. [32], i.e., a suspended rigid cylinder immersed in a flow at a low Reynolds number regime that exhibits non-linear behavior. High-fidelity numerical simulation is used to generate a training dataset that is representative of the problem at hand. The dataset is used to train different elements of the reduced-order model. Further, to evaluate the predictive performance of the current model, a validation profile is used that is significantly different from the one used for training. The predictive performance of the current model is compared with the high-fidelity numerical simulation and reduced-order model that uses polynomial fitting [32].

This paper is organized as follows. Section 2 discusses the overall structure of the model. Section 3 describes the training of the HW model for the force amplitude and modal coefficients of the non-linear corrector term used in the frequency submodel. Section 4 introduces the validation profile and compares the predictive performance of the current model using the HW architecture with the high-fidelity numerical simulation and reduced-order model using polynomial fitting. Section 5 draws the conclusions.

2 Hybrid reduced-order model

2.1 Overall model structure

Following the work of Gallardo et al. [32], the overall model is split into two blocks, one modeling the force exerted by the surrounding fluid on the structure (i.e., force model), and the other modeling the response of the structure to the fluid force (i.e., structural dynamics model). The force model is split into two submodels, one modeling the dominant frequency at which the force is exerted (i.e., frequency model) and the other modeling the force amplitude (i.e., amplitude model). The frequency submodel consists of a linear, time-invariant (LTI) model and a non-linear corrector term. Figure 1 represents the overall structure of the model.

The model has to be trained using a profile that is most representative of the typical inflow condition of the FSI phenomenon of interest. For this reason, the following dataset has to be populated:

- Temporal evolution of the input flow velocity $\tilde{\boldsymbol{u}} = [\tilde{u}_1 \quad \tilde{u}_2 \quad \cdots \quad \tilde{u}_k \quad \cdots \quad \tilde{u}_N]$
- Temporal evolution of the structural displacement $\tilde{\boldsymbol{d}} = [\tilde{d}_1 \quad \tilde{d}_2 \quad \cdots \quad \tilde{d}_k \quad \cdots \quad \tilde{d}_N]$
- Temporal evolution of the velocity vector field $\tilde{\boldsymbol{V}} = [\tilde{\boldsymbol{v}}_1 \quad \tilde{\boldsymbol{v}}_2 \quad \cdots \quad \tilde{\boldsymbol{v}}_k \quad \cdots \quad \tilde{\boldsymbol{v}}_N]$
- Temporal evolution of the vertical force $\tilde{\boldsymbol{F}} = [\tilde{F}_1 \quad \tilde{F}_2 \quad \cdots \quad \tilde{F}_k \quad \cdots \quad \tilde{F}_N]$

where N represents the total number of samples that have been collected. This dataset can be collected either from experimental measurement or high-fidelity numerical simulation. In the current study, the training dataset has been produced through high-fidelity numerical simulation.

2.2 Force model

Gallardo et al. [32] presented the following formulation for the force model:

$$\boldsymbol{x}_{k+1} = A\boldsymbol{x}_k + Bu_k. \tag{2.1}$$

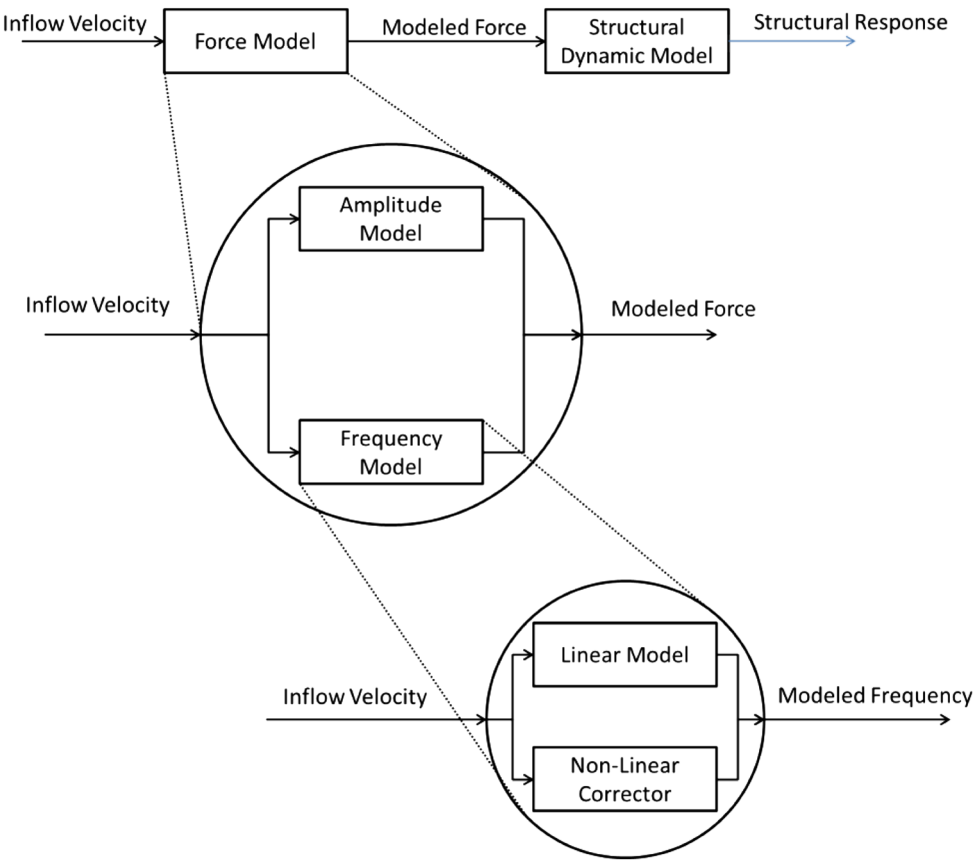

Fig. 1 General structure of the model

$$a_j^k = g_{\text{fr}}^j(u_k, t_k). \tag{2.2}$$

$$\hat{\text{fr}}_k = \tilde{C}\left(\Phi\, \boldsymbol{x}_k + \sum_{j=1}^{P} \boldsymbol{\psi}_j a_j^k\right). \tag{2.3}$$

$$F_{M_K} = f_M(u_k, t_k). \tag{2.4}$$

$$F_k = F_{M_K} \sin(2\pi \hat{\text{fr}}_k\, t_k). \tag{2.5}$$

The overall force signal at a certain time t_k (i.e., F_k) depends on the modeled amplitude F_{M_K} and on the modeled frequency $\hat{\text{fr}}_k$. In Gallardo et al. [32], the force amplitude was modeled by fitting a polynomial, i.e., $f_M(u_k, t_k)$ was a polynomial fit that related the value of the input u_k and time t_k to the value of the force amplitude F_{M_K}.

The frequency was modeled through the use of a hybrid model that would propagate the system states $\boldsymbol{x}_k$ using an LTI model and a non-linear corrector term ($\sum_{j=1}^{P} \boldsymbol{\psi}_j a_j^k$) to account for the non-linearities. The non-linear corrector term was determined through proper orthogonal decomposition (POD) of the difference between the projected states of the LTI system and the original flow field data. In Gallardo et al. [32], the modal coefficients $\boldsymbol{a}^k$ were modeled by fitting a set of polynomial functions $g_{fr}^j(u_k, t_k)$ that would relate the input u_k and time t_k to the value of the modal coefficients $\boldsymbol{a}^k$.

The use of polynomial fitting limits the predictive capability of the overall model, especially when the input is sufficiently different from that used in training the model. For this reason, the current work employs HW architecture with non-linear functions based on a neural network structure with three layers (i.e., input, hidden, and output layers) to model the force amplitude and modal coefficients. The structure of the HW model is described in the next two sections.

2.2.1 *Force amplitude*

For generating model for the force amplitude, it is first necessary to determine the upper envelope of the original force signal $\tilde{\boldsymbol{F}}_u$. Using this and the temporal evolution of the input $\tilde{\boldsymbol{u}}$, it is possible to train a HW model capable of predicting the force amplitude signal F_{M_K} given an input u_k. The HW model is composed of three blocks: a non-linear input block, an intermediate linear block and a non-linear output block [34]. This structure is shown in Fig. 2.

The mathematical formulation of the HW model for the force amplitude is given as follows:

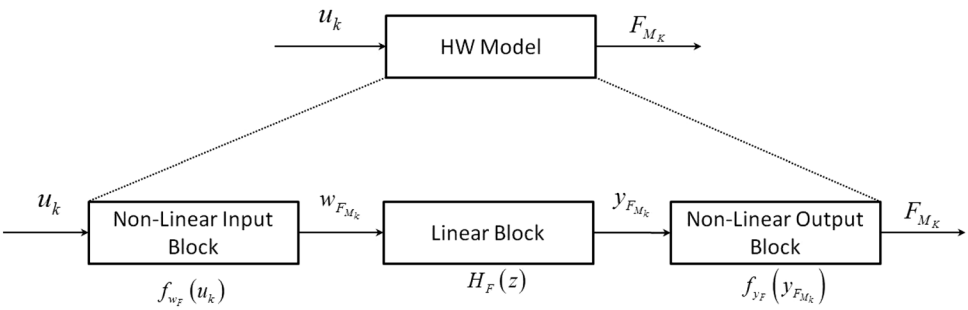

Fig. 2 Schematic representation of the components of the Hammerstein–Wiener model for the force amplitude

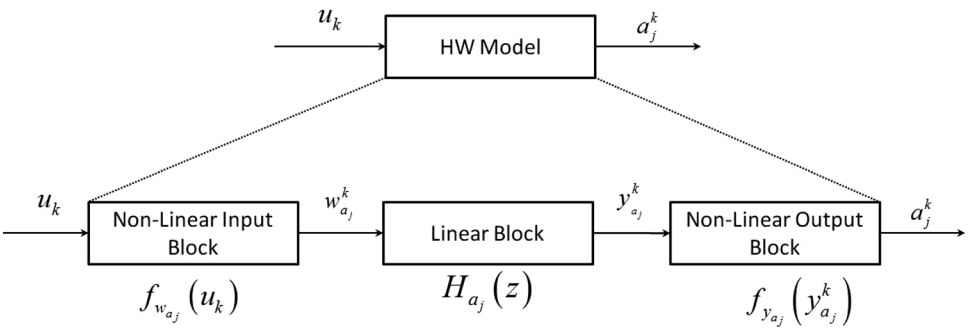

Fig. 3 Schematic representation of the components of the Hammerstein–Wiener model for a modal coefficient

$$
\begin{aligned}
w_{\mathrm{F}M_k} &= f_{w\mathrm{F}}(u_k),\\
y_{\mathrm{F}M_k} &= H_{\mathrm{F}}(z)\cdot w_{\mathrm{F}M_k}\\
&= \left(\frac{1+o_1z^{-1}+o_2z^{-2}+\cdots+o_{n\mathrm{Z}}z^{-n\mathrm{Z}}}{1+p_1z^{-1}+p_2z^{-2}+\cdots+p_{n\mathrm{P}}z^{-n\mathrm{P}}}\right)_F w_{F_{M_k}},\\
F_{MK} &= f_{y\mathrm{F}}\left(y_{\mathrm{F}M_k}\right).
\end{aligned}
\tag{2.6}
$$

The input to the overall HW model is u_k and the output is F_{M_K}. Two non-linear functions constitute the non-linear input ($f_w(u_k)$) and output $\left(f_y\left(y_{\mathrm{F}M_k}\right)\right)$ blocks, which, respectively, map u_k to the input of the linear block $w_{\mathrm{F}M_k}$ and the output of the linear block $y_{\mathrm{F}M_k}$ to F_{M_K}. In general, the non-linear functions in the input and output blocks can assume different forms [37]; however, in this study, an artificial neural network (ANN) has been used. The ANN activation functions are represented by sigmoid functions. Each ANN is composed of three layers (including one hidden layer), and the number of neurons in each layer of the ANN is a key parameter to be established during training of the HW model. Iterative Levenberg-Marquardt algorithm (see Janczak [37]) was used to determine the biases and weights applied to each neuron.

The linear block is represented by a transfer function $H_{\mathrm{F}}(z)$ with a number of poles n_{p} and zeroes n_{z}. The optimal number of poles and zeroes is determined through a procedure discussed later in Sect. 3.

2.2.2 *Modal coefficients of the non-linear corrector*

Similar to the force amplitude model, the current study uses HW model architecture to model the evolution of the modal coefficients (i.e., to relate the input u_k to each of the modal coefficient a_j^k for any given time point). Each modal coefficient is modeled by an HW model, i.e., HW model is different for each modal coefficient in that the number of neurons in the hidden layers of the non-linear input and output ANNs is different and similarly the number of poles and zeroes in the transfer function is different for each HW model. Figure 3 shows the structure of the HW model for the jth modal coefficient a_j^k (related to the mode shape $\boldsymbol{\psi}_j$).

The mathematical formulation of the HW model for a modal coefficient a_j^k is given as follows:

$$
\begin{aligned}
w_{a_j}^k &= f_{w_{a_j}}(u_k),\\
y_{a_j}^k &= H_{a_j}(z)\cdot w_{a_j}^k\\
&= \left(\frac{1+o_1z^{-1}+o_2z^{-2}+\cdots+o_{n\mathrm{Z}}z^{-n\mathrm{Z}}}{1+p_1z^{-1}+p_2z^{-2}+\cdots+p_{n_P}z^{-n_P}}\right)_{a_j} w_{a_j}^k,\\
a_j^k &= f_{y_{a_j}}\left(y_{a_j}^k\right).
\end{aligned}
\tag{2.7}
$$

The input to the HW model is u_k and the output is a_j^k. Two non-linear functions constitute the non-linear input ($f_{w_{a_j}}(u_k)$) and output ($f_{y_{a_j}}\left(y_{a_j}^k\right)$) blocks, which, respectively, map u_k to the input of the linear block $w_{a_j}^k$ and the output of the linear block $y_{a_j}^k$ to a_j^k. Similar to the force

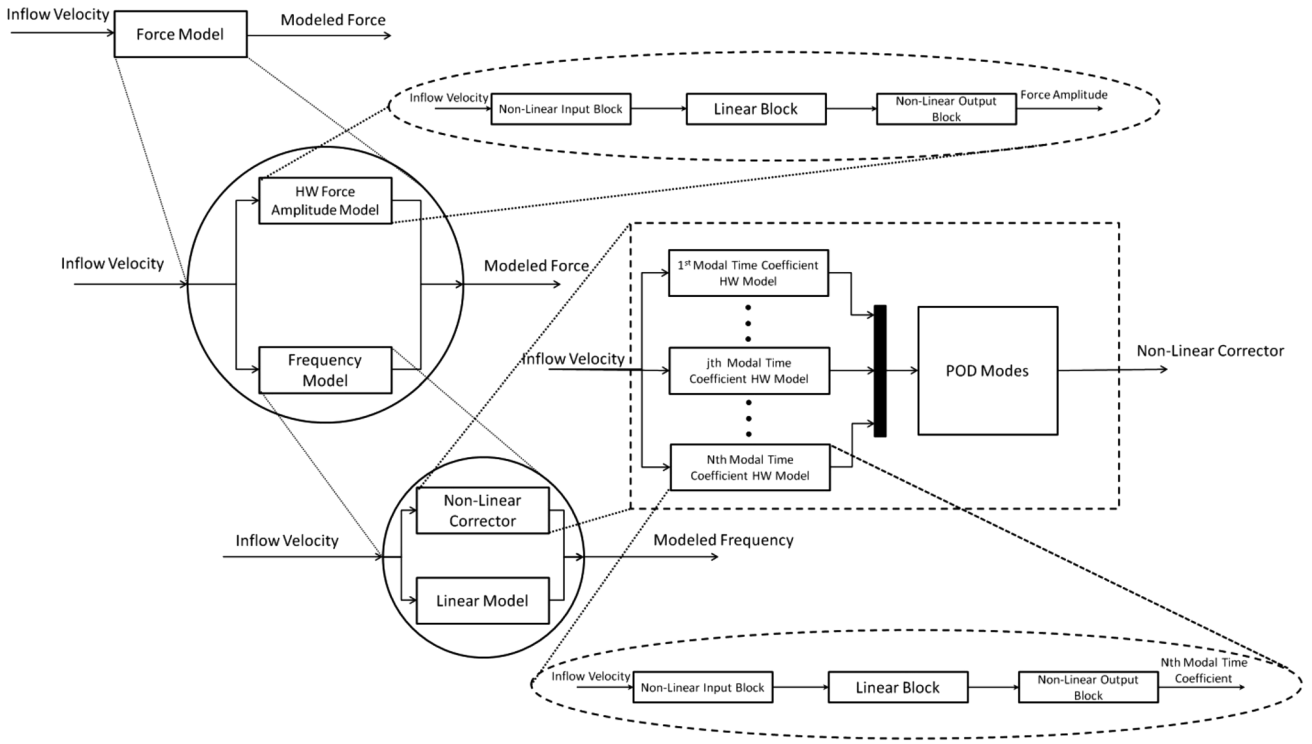

Fig. 4 Overall structure of the force model

amplitude model, the non-linear functions are based on ANNs. As before, the linear block is constituted by a transfer function $H_{a_j}(z)$ with n_p number of poles and n_z number of zeroes.

2.2.3 Summary of force model

The overall model structure of the force model is represented in Fig. 4 and its mathematical formulation is summarized in Eq. 2.8.

$$
\begin{aligned}
&\boldsymbol{x}_{k+1} = A\boldsymbol{x}_k + Bu_k,\\
&\begin{cases}
w_{a_j}^k = f_{w_{a_j}}(u_k),\\
y_{a_j}^k = H_{a_j}(z)\cdot w_{a_j}^k = \left(\dfrac{1+o_1z^{-1}+o_2z^{-2}+\cdots+o_{n_Z}z^{-n_Z}}{1+p_1z^{-1}+p_2z^{-2}+\cdots+p_{n_P}z^{-n_P}}\right)_{a_j} w_{a_j}^k,\\
a_j^k = f_{y_{a_j}}\left(y_{a_j}^k\right),
\end{cases}\\
&\hat{\mathrm{fr}}_k = \tilde{C}\left(\Phi\,\boldsymbol{x}_k + \sum_{j=1}^{P}\boldsymbol{\psi}_j a_j^k\right),\\
&\begin{cases}
w_{\mathrm{F}_{M_k}} = f_{w_{\mathrm{F}}}(u_k),\\
y_{\mathrm{F}_{M_k}} = H_F(z)\cdot w_{\mathrm{F}_{M_k}} = \left(\dfrac{1+o_1z^{-1}+o_2z^{-2}+\cdots+o_{n_Z}z^{-n_Z}}{1+p_1z^{-1}+p_2z^{-2}+\cdots+p_{n_P}z^{-n_P}}\right)_{\mathrm{F}} w_{F_{M_k}},\\
F_{M_K} = f_{y_{\mathrm{F}}}\left(y_{\mathrm{F}_{M_k}}\right),
\end{cases}\\
&F_k = F_{M_K}\sin(2\pi\hat{\mathrm{fr}}_k\, t_k).
\end{aligned}
\tag{2.8}
$$

The force model is made of two blocks related to force amplitude and frequency. The frequency model is a hybrid model that uses an LTI model and a non-linear corrector term. HW model architecture is used for the force amplitude and modal coefficients in the non-linear corrector term. Each HW model consists of three separate blocks including a non-linear input block, an intermediate linear block and a non-linear output block. The non-linear blocks are based on ANNs, while the linear block is a transfer function with a defined number of poles and zeroes. The force model output is used as the input of the structural dynamics model.

2.3 Structural dynamics model

In the current study, the structure is modeled using a mass-spring-damper system as expressed in Eq. 2.9.

$$m\ddot{d}(t) + c\dot{d}(t) + Kd(t) = F(t) \tag{2.9}$$

where m, c and K are the mass, the damping coefficient and the stiffness of the system, respectively. $F(t)$ is the applied force and $d(t)$ is the structural displacement.

The state-space based discrete form of Eq. 2.9 is given as follows:

$$z_{k+1} = \begin{bmatrix} 0 & 1 \\ \frac{K}{m} & \frac{c}{m} \end{bmatrix} z_k + \begin{bmatrix} 0 \\ \frac{1}{m} \end{bmatrix} F_k$$
$$d_k = \begin{bmatrix} 1 \\ 0 \end{bmatrix}^{\mathrm{T}} z_k \tag{2.10}$$

where z_k is the state vector and the two states are the structural displacement and velocity.

3 Model identification

3.1 HW model training

As mentioned in Sect. 2, an HW model is characterized by three blocks (i.e., non-linear input and output blocks and a linear intermediate block). These three blocks are characterized by four parameters:

- The number of poles of the linear transfer function n_{P}
- The number of zeroes of the linear transfer function n_{P}
- The number of neurons in the hidden layer of the ANN for the input block n_{IN}
- The number of neurons in the hidden layer of the ANN for the output block n_{OUT}

Before training the HW model, it is necessary to define these parameters. Ideally, the HW model should be as accurate as possible while being as efficient as possible. However, efficiency and accuracy result in a trade-off in that an accurate model will use a larger number of neurons, poles and zeroes whereas an efficient model would use as few as possible.

In this study, a normalized root mean square error (NRMSE) fit value [38] is used as a cost function to compare the accuracy of the different models (i.e., of models that have different number of neurons, poles and zeroes). Equation 3.1 expresses how the NRMSE is determined for the HW model for the force amplitude, while Eq. 3.2 expresses how it is determined for the HW models for the modal coefficients.

$$\mathrm{NRMSE}_{\mathrm{FIT}}^{\mathrm{F}} = \left(1 - \frac{\left\|\tilde{\boldsymbol{F}}_u - \boldsymbol{F}_M\right\|_2}{\left\|\tilde{\boldsymbol{F}}_u - \bar{\tilde{\boldsymbol{F}}}_u\right\|_2}\right) \cdot 100 \tag{3.1}$$

where $\boldsymbol{F}_M$ is the temporal evolution of the modeled amplitude while $\tilde{\boldsymbol{F}}_u$ is the average of the upper envelope of the original force signal $\tilde{\boldsymbol{F}}_u$.

$$\mathrm{NRMSE}_{\mathrm{FIT}}^{j} = \left(1 - \frac{\left\|\tilde{\boldsymbol{a}}_j - \boldsymbol{a}_j\right\|_2}{\left\|\tilde{\boldsymbol{a}}_j - \bar{\tilde{\boldsymbol{a}}}_j\right\|_2}\right) \cdot 100 \tag{3.2}$$

where $\boldsymbol{a}_j$ is the temporal evolution of the modeled j^{th} modal coefficient while $\bar{\tilde{\boldsymbol{a}}}_j$ is the average of the original modal coefficient $\tilde{\boldsymbol{a}}_j$.

The NRMSE is a measure of how precisely a model approximates the original data. It can go from $-\infty$ (poor fit) to 100 (perfect fit). If the NRMSE is equal to 0, it means that the model is equivalent to taking the average of the original data. Any value between 0 and 100 indicates that the model is better than using the average of the original data.

The current study proposes a training method that first determines the number of poles and zeroes in the linear block, assuming that no non-linear blocks are present. Subsequently, the method determines the number of neurons in the hidden layers of the input and output ANN using the linear model found in the previous step.

For the characterization of the linear model, a complexity limit is established. This is done by defining a maximum number of poles that the transfer function can have (the maximum number of zeroes will be smaller or equal to the maximum number of poles). Once the complexity limit is established, an algorithm generates a sequence of models with increasing complexity (i.e., with an increasing number of poles and zeroes) and determines the NRMSE value for each model.

The generated models that share the same number of poles (with different number of zeroes) are grouped in sets. For each set, the model with the highest NRMSE is selected, i.e., the best model in each set. The best models among all sets are compared using their NRMSE values and the linear model with a certain NRMSE value is selected.

Figure 5 represents the algorithm that generates the linear models with increasing complexity, while Fig. 6 represents the selection procedure described above.

After this procedure, a linear model with a defined number of poles and zeroes is selected. The next step towards the full characterization of the HW model consists of determining the number of neurons in the hidden layer of the input and output ANNs. To do so, a procedure similar to the one adopted for the force amplitude is used. A complexity limit for the input non-linear block is established while the complexity of the output non-linear block is set to be equal or less than that of the input non-linear block. This is done by defining the maximum number of neurons that the input neural network can have, where the maximum number of neurons in the output neural network will be smaller than or equal to that in the input block. Once the complexity limit is established, an algorithm generates models with increasing complexity (i.e., with an increasing number of neurons in the input and output neural networks) and determines for each model its NRMSE value.

Similar to the procedure described for the linear component of the HW model, the generated models that share

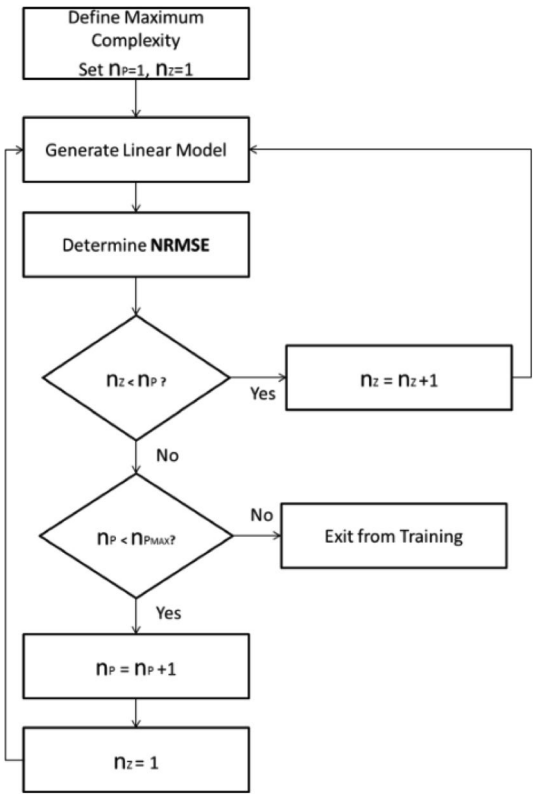

Fig. 5 Representation of the algorithm used to generate linear models with increasing complexity

the same number of neurons in the input block are grouped into sets. The models in each set share the number of neurons in the input block but have different number of neurons in the output block. As before, for each set the model with the highest NRMSE value is selected, i.e., the best model in each set. The best models from each set are then compared using their NRMSE values and the model with a certain NRMSE value is selected.

The steps of the algorithm that generate the models with increasing complexity (i.e., the models with increasing number of neurons in the input and output non-linear blocks) are similar to that used for the linear model, which is depicted in Fig. 5. Similarly, the method that is used to extract the best model in each set and to select the final model is similar to that depicted in Fig. 6. By following the above procedures, the number of poles, zeroes, and neurons is selected that lead to a suitable HW model for both the force amplitude and modal coefficients in the non-linear corrector term of the frequency model.

3.2 Training dataset

As stated in Sect. 2, the model has to be trained using a dataset that is most representative of the input flow condition that is encountered in the FSI problem of interest. In the current study, the same FSI problem setup of Gallardo et al. [32] is selected.

The setup consists of a two-dimensional rigid cylinder suspended in a flow at a low Reynolds number regime that exhibits a non-linear behavior (i.e., between $Re = 90$ and 125). The cylinder is allowed to oscillate only along the direction orthogonal to the flow. The cylinder motion is governed by its mass $m = 9.5328\text{e}{-4}$ kg, damping coefficient $c = 1.04\text{e}{-4}$ kg/s and stiffness $K = 1.8528$ N/m. The cylinder diameter D is equal to $1.6\text{e}{-3}$ m. Figure 7 represents the problem setup.

The input profile (i.e., the inflow velocity profile) consists of incremental velocity steps. Figure 8 represents the high-fidelity numerical simulation results in terms of fluid force and structural displacement for the given input profile. The dotted vertical line represents the temporal location when the lock-in phenomenon is triggered, causing an exponential growth in the structural displacement.

3.3 Model training and identification

The dataset developed with the high-fidelity numerical simulation, as described in Sect. 3.2, is used to identify the model.

3.3.1 Training: force amplitude

The upper envelope of the original force signal $\tilde{\boldsymbol{F}}_u$, together with the temporal evolution of the input $\tilde{\boldsymbol{u}}$, was used to train the linear block of the HW model for the force amplitude. This was done following the procedure described in Sect. 3.1. The maximum complexity was established to be 30 poles (and consequently 30 zeroes). Figure 9 represents the NRMSE value of the best model in each set, where each set is associated with a different number of poles.

Figure 9 shows that models with more than five poles lead to marginal or no improvement in the NRMSE value. For this reason, linear intermediate block with five poles is selected. The best model in the set with five poles was the one with three zeroes, as shown in Fig. 10.

Using the same input signal of the training dataset, the characterized linear model has been used to determine the force amplitude signal. Figure 11 shows the modeled force amplitude versus the original data.

Figure 11 shows that the linear intermediate block is able to successfully capture the overall behavior but fails in effectively capturing the transients. Therefore, non-linear blocks were identified next to fully characterize the HW model for the force amplitude.

The maximum complexity for the non-linear blocks was established to be of 50 neurons (both in the input and

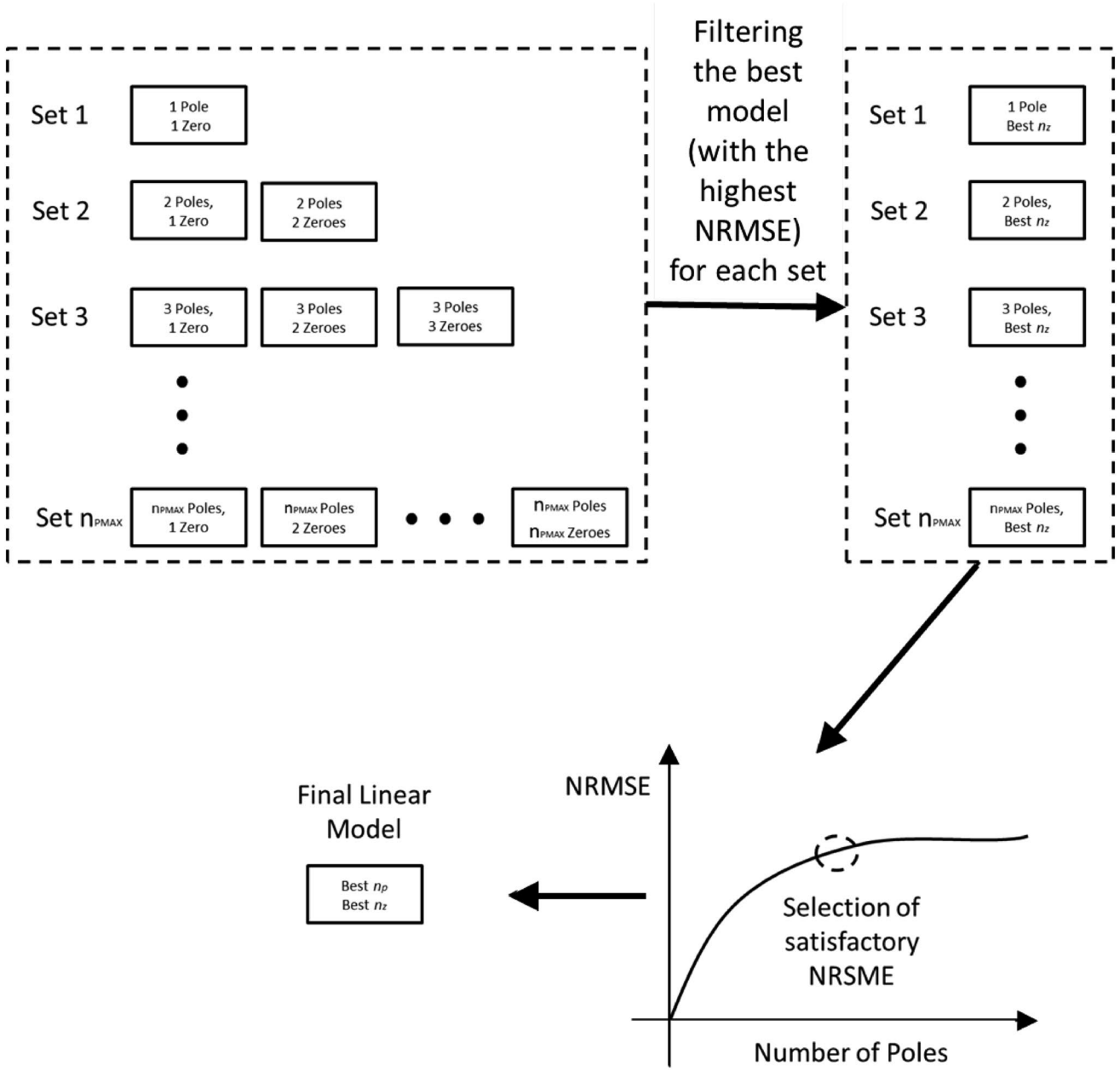

Fig. 6 Method to select the linear block of an HW model

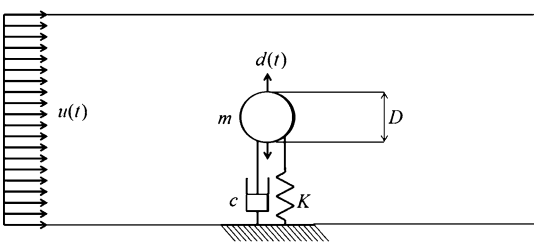

Fig. 7 Schematic of the FSI problem setup

output blocks). The algorithm described in Sect. 3.1 was used to produce 50 different sets of models, where models in a given set have the same number of neurons in the input block but with different number of neurons in the output block. Figure 12 shows the NRMSE value of the best model in each set.

Figure 12 shows that using five neurons in the hidden layer of the input ANN is sufficient for this particular FSI problem. The NRMSE values of the models in this set are shown in Fig. 13. All models result in similar NRMSE

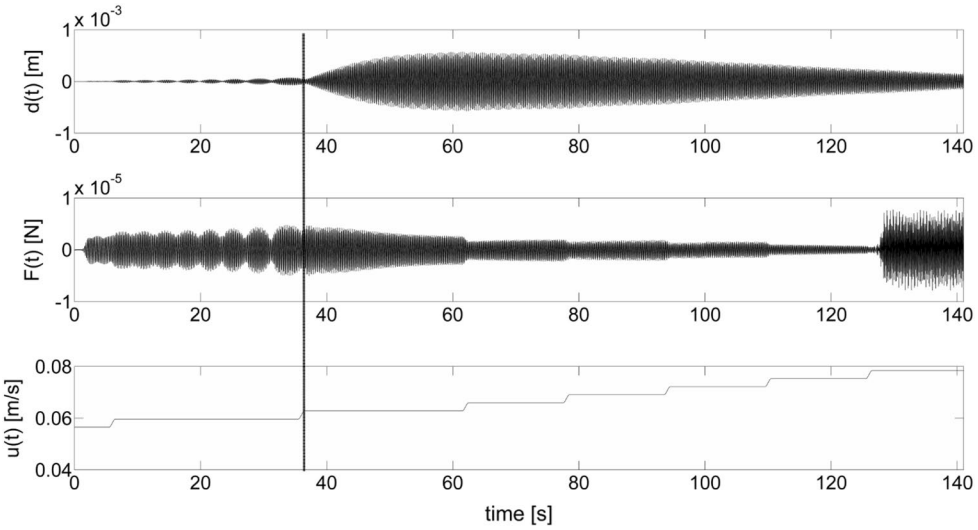

Fig. 8 Training dataset. *Top* structural displacement. *Middle* force signal. *Bottom* input velocity. The *vertical line* across all graphs represents the temporal location where the lock-in phenomenon is triggered (at $Re = 100$)

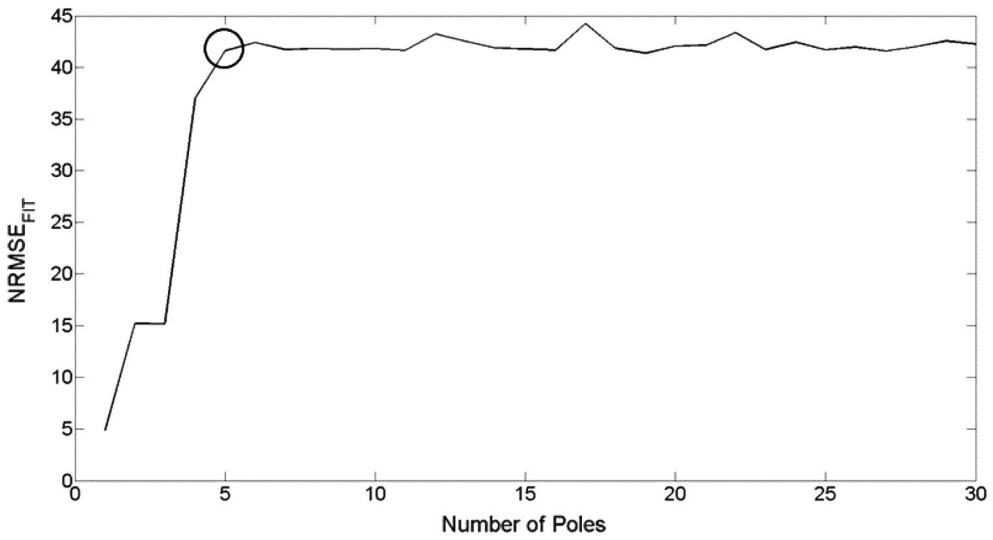

Fig. 9 NRMSE value of the best model in each set for the linear intermediate block in the force amplitude model

value; however, the one with two neurons in the output block is better than others.

Considering the linear intermediate and non-linear input and output blocks identified above, the final HW model of the force amplitude is as follows: five neurons in the hidden layer of the ANN associated with the input non-linear block, followed by a transfer function (linear intermediate block) with five poles and three zeroes, and an output non-linear block with two neurons in its hidden layer. This model was tested on the training input profile $\tilde{\boldsymbol{u}}$ and Fig. 14 shows the modeled force amplitude versus the original signal. Figure 14 shows that the HW model is more effective than the model with only the linear block (latter was shown in Fig. 11). This is also evident in Figs. 10 and 13, which show an increment of about 40 % in the NRMSE value between the model with only the linear block and the final HW model with both linear and non-linear blocks.

3.3.2 Training: modal coefficients in the non-linear corrector term

The current study utilizes nine modes (and related modal coefficients) to model the non-linear component of the frequency model. This is done because the nine modes allow to capture more than 98 % of the energy associated with the frequency model. This section discusses the training process only for the first modal coefficient (with the highest energy content), in which the number of poles, zeroes and neurons is determined. For all the modal coefficients, results are summarized in Table 1.

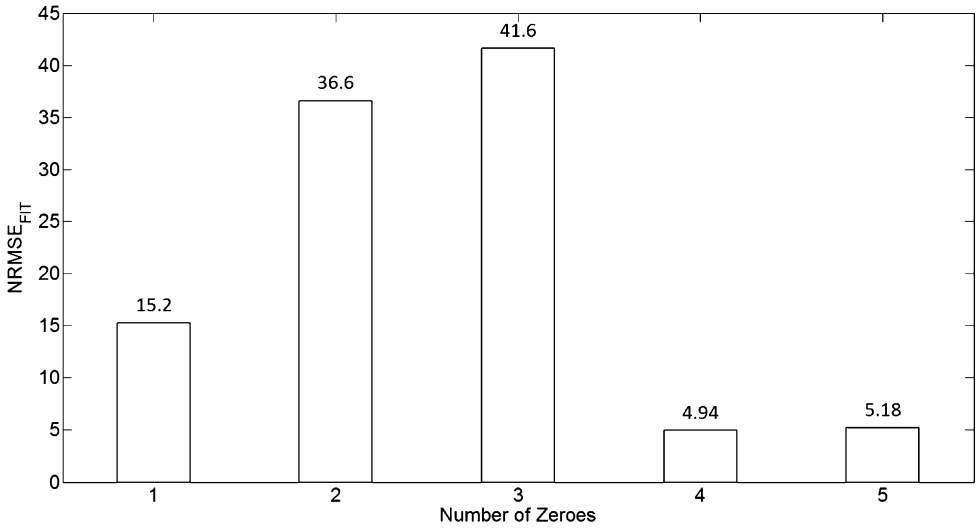

Fig. 10 NRMSE value of the models in the set with five poles for the linear intermediate block in the force amplitude model

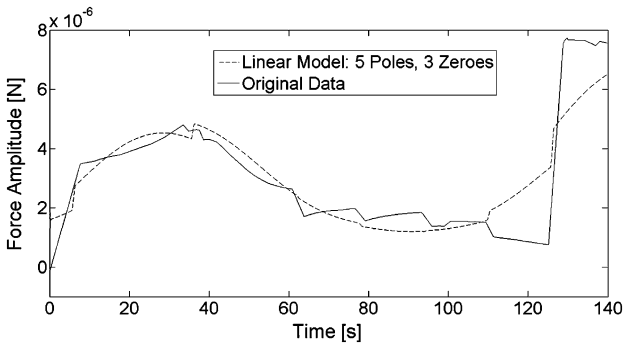

Fig. 11 Original and modeled evolution of the force amplitude using only the linear intermediate block with 5 poles and 3 zeroes

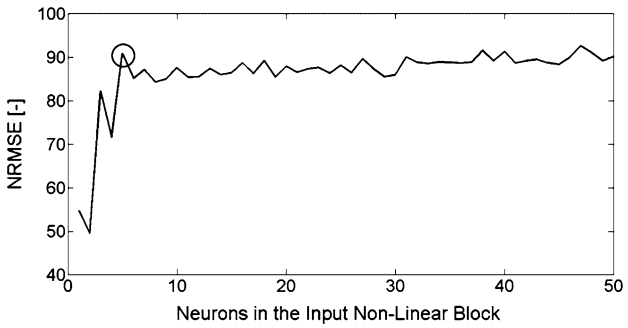

Fig. 12 NRMSE value of the best HW model in each set for the non-linear input and output blocks in the force amplitude model

The procedure followed to train the HW model for modal coefficients is similar to that used for the HW model for the force amplitude, as described in Sect. 3.1. As a first step, the linear block was characterized, where linear models with increasing complexity were generated and separated in different sets. Each set consisted of models with the same number of poles (but different number of zeroes). The best model in each set (i.e., the model with the highest NRMSE value) was selected to represent the set. Figure 15 compares the best model from each set.

Figure 15 shows that models with more than two poles bring only a marginal improvement in the NRMSE value. In the set of models with two poles, the one with two zeroes was found to be the best, as shown in Fig. 16.

Using the same input signal of the training dataset, the characterized linear model has been used to determine the first modal coefficient. Figure 17 shows the modeled modal coefficient versus the original data.

Similar to what was observed for the force amplitude model, the linear block-based model is able to successfully capture the overall behavior but fails in effectively capturing the transients. Moreover, it also fails in capturing the oscillations in the initial phase (between $t = 0$ and 40 s).

The next step involved the characterization of the input and output non-linear blocks. Using the algorithms described in Sect. 3.1, models with increasing number of neurons in the hidden layers of the ANN of the input and output blocks were generated. A maximum complexity was established to be 50 neurons (both in the ANN of the input and output non-linear blocks). The models that shared the same number of neurons in the ANN of the input non-linear block were grouped in the same set. Figure 18 shows the best model (i.e., the model with the highest NRMSE value) in each set. This figure shows that 14 neurons in the input non-linear block are sufficient. The NRMSE values of the models in the set with 14 neurons are presented in Fig. 19.

Figure 19 shows that, in the set with 14 neurons, the output block with 12 neurons results in the highest NRMSE value while several others are close.

Considering the linear intermediate and non-linear input and output blocks above, the final HW model of the first

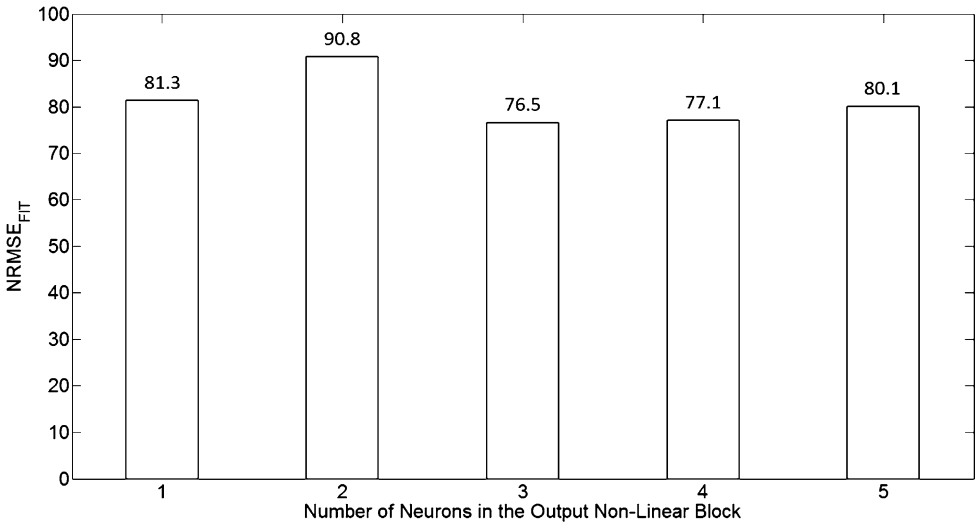

Fig. 13 NRMSE value of the models in the input block set with five neurons for the non-linear input and output blocks in the force amplitude model

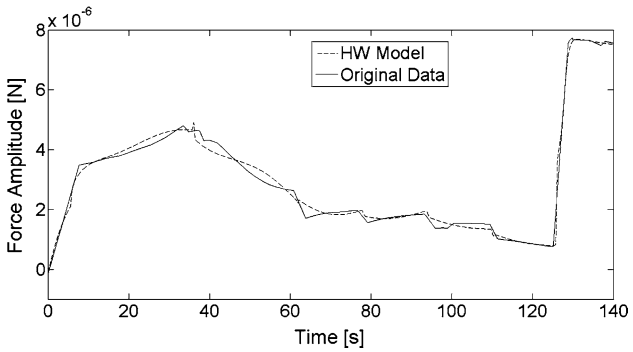

Fig. 14 Original and modeled evolution of the force amplitude with the identified HW model

modal coefficient is as follows: fourteen neurons in the input non-linear block, followed by a transfer function (linear intermediate block) with two poles and two zeroes, and an output non-linear block with twelve neurons. This model was tested on the training input profile $\tilde{\boldsymbol{u}}$ and Fig. 20 shows the modeled modal coefficient versus the original signal.

Figure 20 shows that the identified HW model for the first modal coefficient follows closely the original data. Although it fails to capture the oscillations that are present in the initial phase of the original signal (between $t = 0$ and 40 s), it is able to effectively capture the transient behavior at other locations. Its better performance as compared to the model with only the linear block is quantified by its better NRSME value shown in Figs. 19 and 16 with values about 91 and 79 %, respectively. HW models for other modal coefficients were identified in the same way as the first modal coefficient. The identified model for each modal coefficient is summarized in Table 1.

3.4 Comparison of original and modeled force and displacement

The same input profile $\tilde{\mathbf{u}}$ that was used for the training is used as the input to the overall model identified above. This was done to compare the modeled force and displacement with the original data. Figure 21 compares the force signal.

Table 1 Structure of the HW model for all nine modal coefficients

Modal coefficient	Input non-linear block	Intermediate transfer function		Output non-linear block
	Number of neurons	Number of poles	Number of zeroes	Number of neurons
1st	14	2	2	12
2nd	2	2	1	2
3rd	8	4	2	2
4th	13	9	5	13
5th	6	3	1	1
6th	8	12	4	8
7th	4	10	8	1
8th	11	4	2	1
9th	10	3	3	4

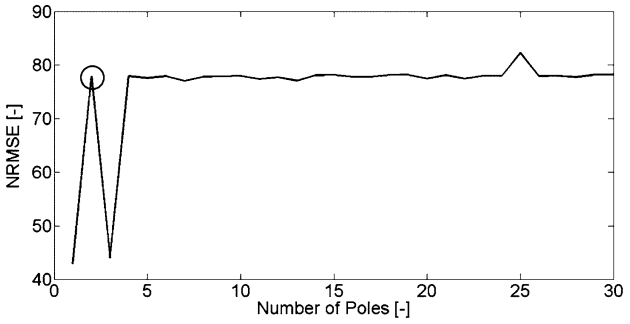

Fig. 15 NRMSE value of the best model in each set for the linear intermediate block of the first modal coefficient

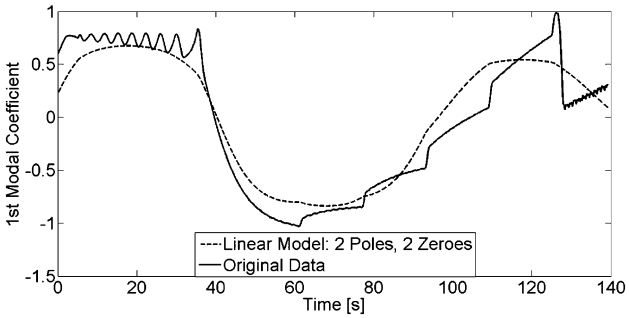

Fig. 17 Original and modeled evolution of the first modal coefficient using only the linear intermediate block with 2 poles and 2 zeroes

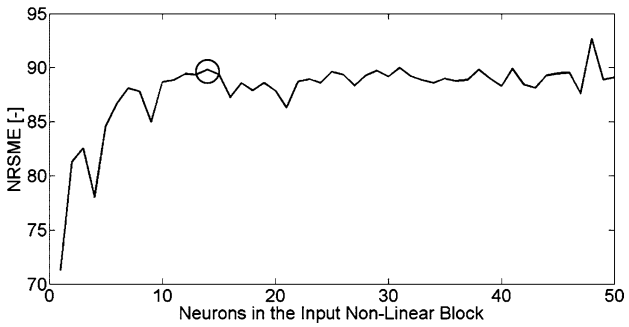

Fig. 18 NRMSE value of the best HW model in each set for the non-linear input and output blocks of the first modal coefficient

Figure 21 shows that the modeled force closely follows the original force signal from the high-fidelity numerical simulation although it fails in identifying the beating profile in the initial phase between $t = 0$ and 40 s. A probable cause is that the non-linear corrector term in the frequency model failed in capturing the oscillations in the first modal coefficient (see Fig. 20). The modeled force was given as the input to the structural model and the resulting displacement is shown in Fig. 22.

As in the case of the force signal, Fig. 22 shows that in the initial phase between $t = 0$ and 40 s the identified model fails in capturing the beating profile in the displacement while after $t = 40$ s the modeled signal closely follows the original data from the high-fidelity numerical simulation.

4 Model validation

4.1 Validation profile

The performance of the model was evaluated through the use of a validation profile which presented a different temporal evolution of the input velocity from that used in training. The validation profile consists of a shifted profile as compared to the one used in training, where the input starts from $Re = 90$ but grows in steps that are 50 % bigger than the ones used in the training profile. Figure 23 shows the validation profile compared with the training profile in a time window up to $t = 58.2$ s (the training profile had a longer duration). Note that the step changes in input

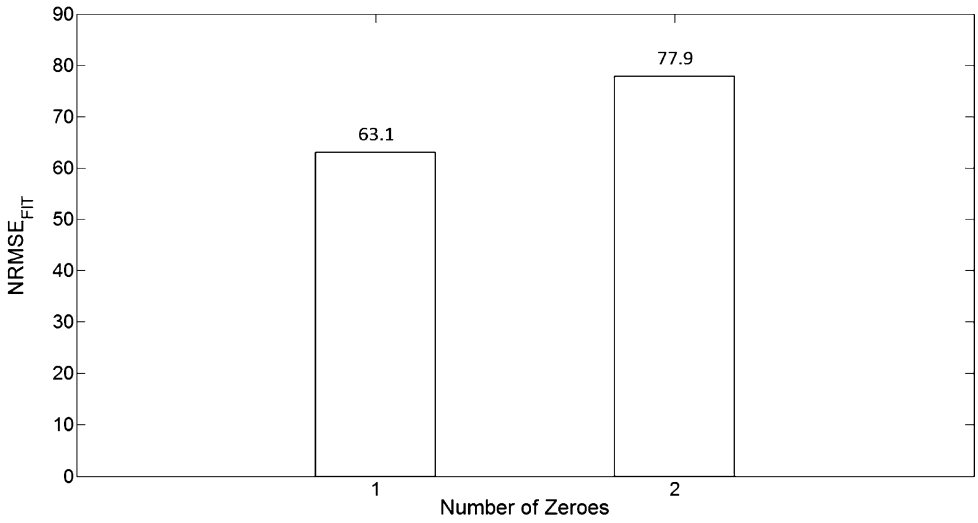

Fig. 16 NRMSE value of the models in the set with two poles for the linear intermediate block of the first modal coefficient

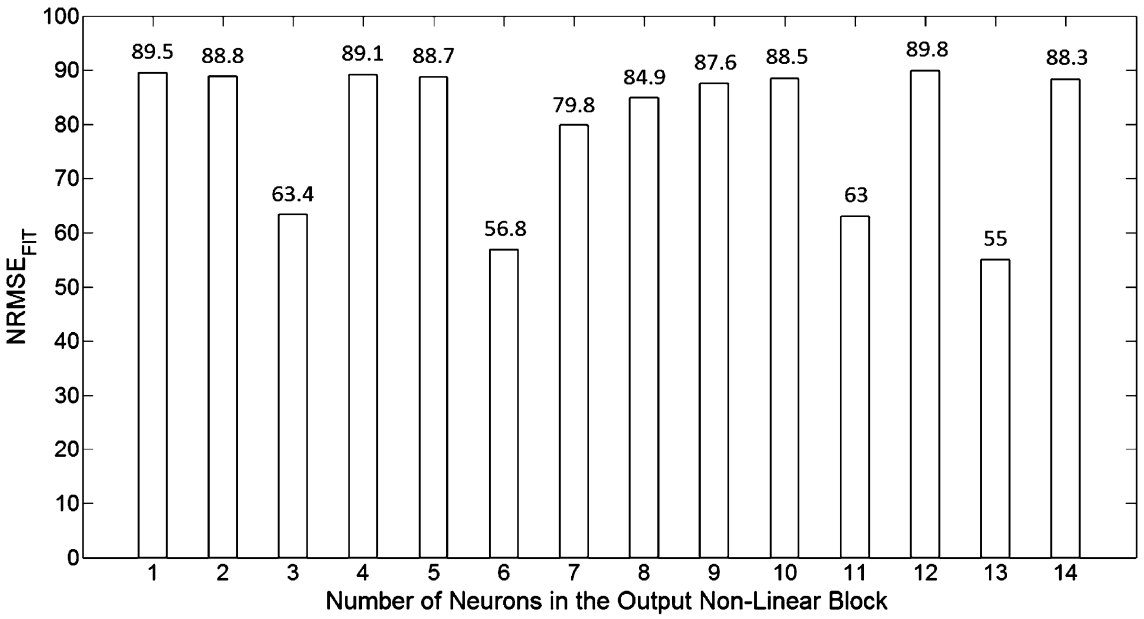

Fig. 19 NRMSE value of the models in the input block set with fourteen neurons for the non-linear input and output blocks of the first modal coefficient

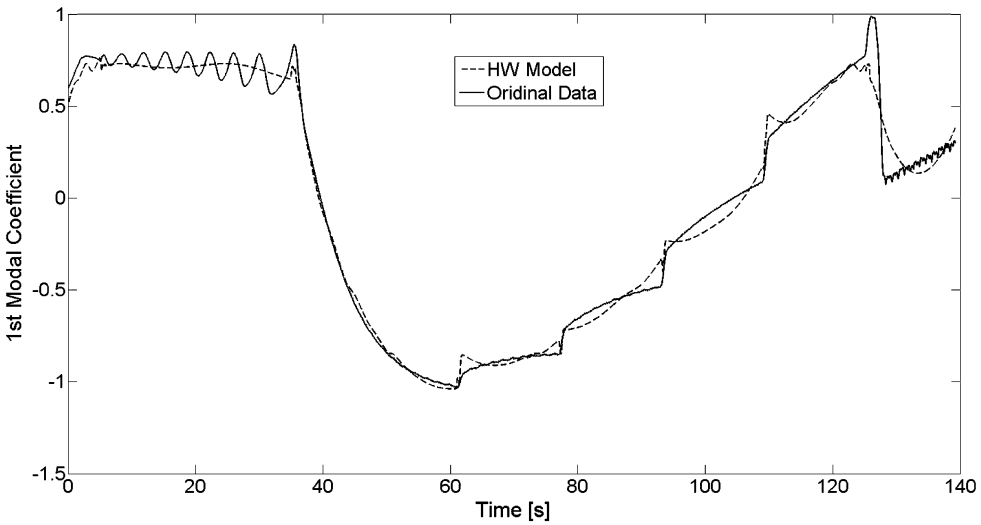

Fig. 20 Original and modeled evolution of the first modal coefficient with the identified HW model

velocity are at the same temporal locations (of $t = 6$ and 36 s) between the training and validation profiles.

The validation profile still presents lock-in phenomenon conditions around $t = 6.5$ s, where the input velocity reaches a value of 0.06275 m/s (corresponding to a *Re* of 100). This input value triggered the lock-in phenomenon during training. This will be further evident in the next section.

4.2 Validation dataset

The validation profile shown in Fig. 23 was used as the input to the high-fidelity numerical simulation. Subsequently, the numerical simulation produced a dataset (validation dataset) comprising the temporal evolution of the force signal and structural displacement. This dataset is presented in Fig. 24.

Figure 24 shows that the lock-in phenomenon is triggered at about $t = 6.5$ s, when the input velocity reaches a value of 0.06275 m/s corresponding to a *Re* of 100. The exponential growth of the structural displacement continues until about $t = 35.3$ s, which corresponds to the next change in the input velocity.

The validation dataset constitutes an interesting validation case because it still presents highly non-linear behavior but with a significantly different temporal evolution.

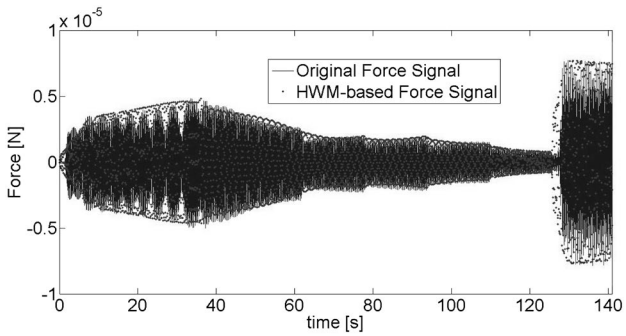

Fig. 21 Original and modeled force signals for the training input profile

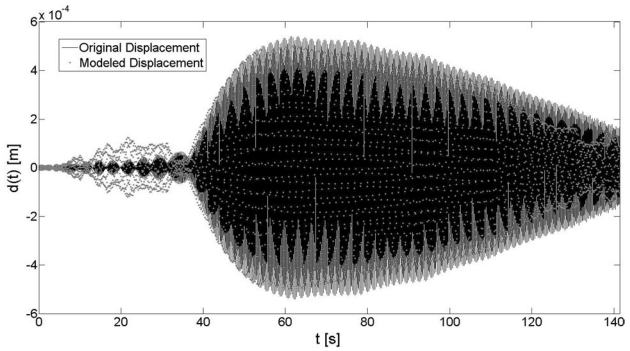

Fig. 22 Original and modeled displacement signals for the training input profile

Similar to what was observed for the training profile, the structural displacement presents a memory that keeps the value of the displacement significantly high even when the frequency of force signal is not close to the natural frequency of the structure.

4.3 Model performance

The validation profile shown in Fig. 24 was used as the input to the trained/identified model. The predicted force and displacement are compared with the high-fidelity simulation data. Here, the predicted force and displacement obtained using a polynomial-based model by Gallardo et al. [32] are also compared. This comparison is shown in Figs. 25 and 27 for the force and structural displacement, respectively.

Figure 25 shows that the polynomial-based model predicts the force magnitude to be consistently higher than the high-fidelity simulation data. It also exhibits a large change around the lock-in region (i.e., from $t = 6.5$ s) instead of a gradual change as observed in the high-fidelity simulation data, while the HW-based model provides a better prediction. To further analyze the lock-in region, Fig. 26 shows the temporal location of the local peaks in the force signal between $t = 8.5$ and $t = 9.5$ s. The first peak after $t = 8.5$ s is observed at about $t = 8.6$ s (i.e., Peak Index 1), which matches between the two models and with the high-fidelity simulation data. At the second peak (i.e., Peak Index 2), a marginal deviation is observed in the polynomial-based model while a good agreement is seen between the HW model and high-fidelity simulation data. A similar trend continues (except at Peak Index of 3) and the deviation in the polynomial-based model prediction becomes significant by the seventh/last peak (i.e., just before $t = 9.5$ s). This behavior is due to the inaccurate prediction of the force frequency by the polynomial-based model. This further shows that the HW-based model provides a significantly better prediction for the force.

Figure 27 shows that the displacement predicted by the HW-based model is also significantly better than that from the polynomial-based model. The HW-based model

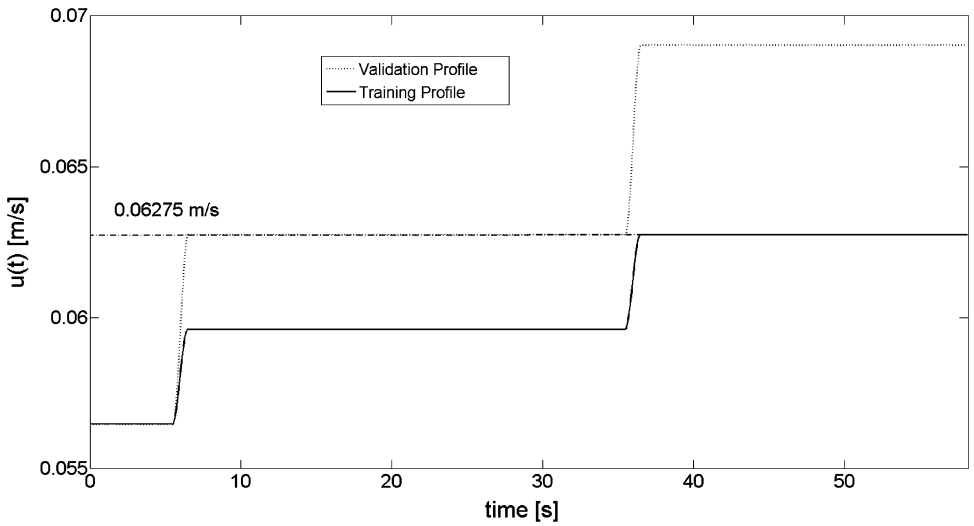

Fig. 23 Validation and training input profiles

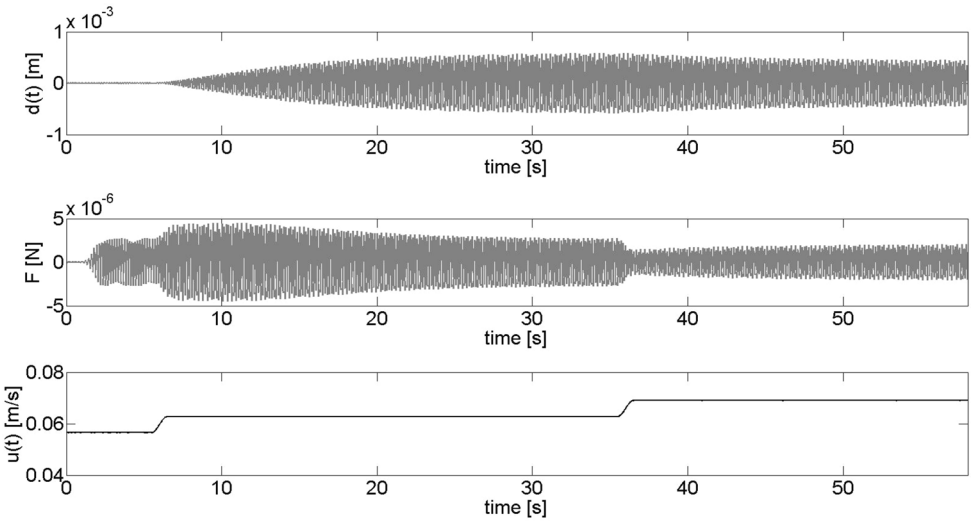

Fig. 24 Validation dataset. *Top* structural displacement. *Middle* force signal. *Bottom* input velocity

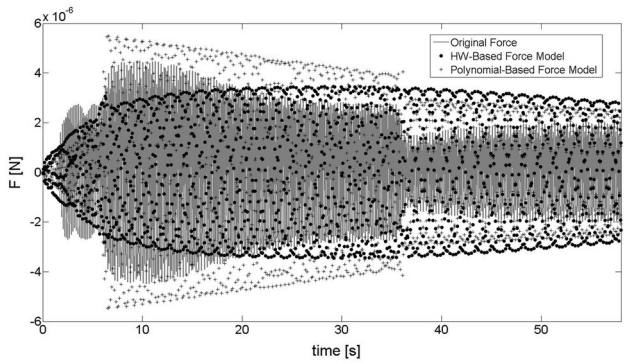

Fig. 25 High-fidelity (original) force signal from validation dataset compared with the predicted force signal from models based on HW architecture and polynomial fitting

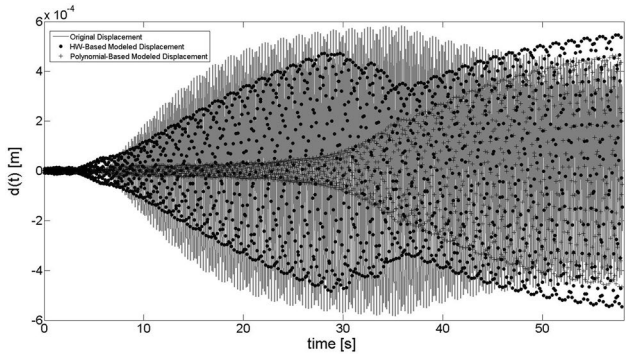

Fig. 27 High-fidelity (original) structural displacement from validation dataset compared with the predicted displacement from models based on HW architecture and polynomial fitting

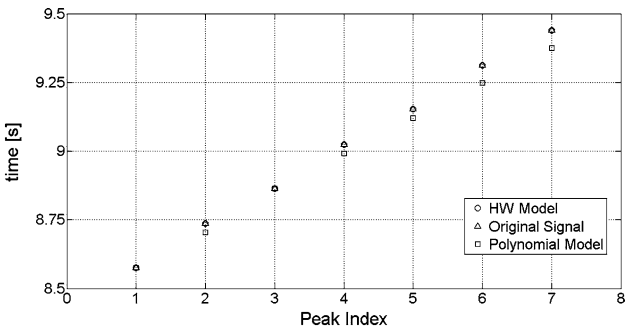

Fig. 26 Temporal location of the local peaks in the high-fidelity (original) force signal from validation dataset as compared with the predicted location from models based on HW architecture and polynomial fitting in a time window between $t = 8.5$ and $t = 9.5$ s

effectively captures the exponential growth, although the amplitude is slightly smaller, as compared to the high-fidelity simulation data. The HW model also detects when the lock-in phenomenon begins and ends. In contrast, the displacement predicted by the polynomial-based model fails in capturing the exponential growth caused by the lock-in phenomenon. Given that the force amplitude predicted by this model was comparable with the high-fidelity one, as shown in Fig. 25, the cause for such a poor prediction of displacement prediction is due to an inaccurate prediction of the force frequency by the polynomial-based model, as shown in Fig. 26. In the prediction by the polynomial-based model, the exponential growth in displacement starts at about $t = 30$ s and reaches values that are of the same order as the high-fidelity simulation data at about $t = 55$ s.

5 Conclusions

In this study, we tested the predictive capability of a fluid–structure interaction model based on a HW architecture with non-linear blocks modeled employing ANNs

with one hidden layer. The overall model contains two blocks related to the force signal and structural response. The force model consists of two submodels, i.e., one for the amplitude and one for the frequency. Frequency submodel contains an input/output linear model and a non-linear corrector term. With the current model structure, the HW modeling technique is applied to the force amplitude and modal coefficients in the non-linear frequency corrector term. Note that the previous study by Gallardo et al. [32] employed polynomial fitting for the same components. HW model for any given variable was composed of three blocks: non-linear input and output blocks and a linear intermediate block. The input and output blocks used an ANN while the linear intermediate block was represented by a transfer function. Structure of each block used in the HW model was discussed. The associated parameters (number of poles, zeroes, and neurons in the hidden layer of the ANN) were identified using a training profile, and the selection was made using the NRMSE fit value.

The current model was tested on the same case study that was investigated by Gallardo et al. [32], i.e., a rigid cylinder suspended in a flow at a low Reynolds number regime. The overall behavior of the predicted force amplitude was similar for both the HW- and polynomial-based models (i.e., for the validation input profile). However, HW-based model showed significantly better predictions in structural displacement. The HW-based model effectively captured the exponential growth in displacement, although the amplitude was smaller, as compared to the original signal. The HW-based model also detected when the lock-in phenomenon begins and ends.

References

1. Larsen A (2000) Aerodynamics of the Tacoma narrows bridge—60 years later. Struct Eng Int 10(6):243–248
2. Kareem A, Kijewski T, Tamura Y (1999) Mitigation of motions of tall buildings with specific examples of recent applications. J Wind Struct 2:201–251
3. Lin N, Letchford C, Tamura Y, Liang B, Nakamura O (2005) Characteristics of wind forces acting on tall buildings. J Wind Eng Ind Aerodyn 93:217–242
4. Tamura Y, Kawasana S, Nakamura O, Kanda J, Nakata S (2006) Evaluation perception of wind-induced vibration in buildings. Proc Inst Civ Eng Struct Build 159(5):283–293
5. Bashor R, Kijewsky-Correa T, Kareem A (2005) On the wind-induced response of tall buildings: the effect of uncertainties in dynamic properties and human comfort thresholds. In: Proceedings of 10th Americas conference on wind engineering, Baton Rouge, Louisiana
6. Kareem A (1987) Wind effects on structures: a probabilistic viewpoint. Probab Eng Mech 2(4):166–200
7. Tse KT, Hitchcock PA, Kwok KCS, Thepmongkorn S, Chen CM (2009) Economic perspectives of aerodynamic treatments of square tall building. J Wind Eng Ind Aerodyn 97:455–467
8. Kwok KCS, Wilhelm PA, Wilkie BG (1988) Effect of edge configuration on wind-induced response of tall buildings. Eng Struct 10(2):135–140
9. Menicovich D, Vollen J, Amitay M, Letchford C, Dyson A, DeMauro E, Ajith R (2012) A different approach to the aerodynamic performance of tall buildings. In: Council on tall buildings and Urban habitat issue IV
10. Jonkman JM, Matha D (2011) Dynamics of offshore floating wind turbines analysis of three concepts. J Wind Energy 14:557–569
11. Ham ND, Garelick MS (1968) Dynamic stall considerations in helicopter rotors. J Am Helicopt 13(2):49–55
12. Ham ND (1968) Aerodynamic loading on a two-dimensional airfoil during dynamic stall. AIAA J 6(10):1927–1934
13. McCroskey WJ, Carr LW, McAlister KW (1976) Dynamic stall experiments on oscillating airfoils. AIAA J 14(1):57–63
14. Dowell EH, Hall KC (2001) Modeling of fluid–structure interaction. Annu Rev Fluid Mech 33:445–490
15. Theodorsen T, Garrick IE (1933) General potential theory of arbitrary wing sections. NACA Report No. 452
16. Dowell EH, Crawley EF, Curtiss HC Jr, Peters DA, Scanlan RH, Sisto F (1995) A modern course in aeroelasticity, 3rd ed. Kluwer Acad. Pub., Dordrecht
17. Florea R, Hall KC, Cizmas PG (1998) Reduced-order modeling of unsteady viscous flow in a compressor cascade. AIAA J 36(6):1039–1048
18. Tijdeman H, Seebass R (1980) Transonic flow past oscillating airfoils. Annu Rev Fluid Mech 12(1):181–222
19. Seebass AR, Fung KY, Przybytkowski SM (1986) Advances in the understanding and computation of unsteady transonic flow. Recent advances in aerodynamics. Springer, New York, pp 3–37
20. Nixon D (1989) Unsteady transonic aerodynamics. In: Progress in Astronautics and Aeronautics, vol 120. AIAA, Washington DC
21. Benaroya H, Gabbai RD (2007) Modeling vortex-induced fluid–structure interaction. Philos Trans R Soc 366:1231–1274
22. Karhunen Kari (1947) Über lineare Methoden in der Wahrscheinlichkeitsrechnung. Ann Acad Sci Fennicae Ser A I Math Phys 37:1–79
23. Loève M (1978) Probability theory II. In: Graduate Texts in Mathematics, vol 46. Springer, Berlin
24. Berkooz G, Holmes P, Lumley JL (1993) The proper orthogonal decomposition in the analysis of turbulent flows. Annu Rev Fluid Mech 25:539–575
25. Aradag S, Siegel S, Seidel J, Cohen K, McLaughlin T (2011) Filtered POD-based low dimensional modeling of the 3D turbulent flow behind a circular cylinder. Numer Meth Fluids 66:1–16
26. Seidel J, Siegel S, Fagley C, Cohen K, McLaughlin T (2009) Feedback control of a circular cylinder wake. J Aerosp Eng 223:379–392
27. Siegel SG, Seidel J, Fagley C, Luchtenburg DM, Cohen K, McLaughlin T (2008) Low-dimensional modeling of a transient cylinder wake using double proper orthogonal decomposition. J Fluid Mech 610:1–42
28. Siegel SG, Cohen K, Seidel J, McLaughlin T (2007) State estimation of transient flow fields using double proper orthogonal decomposition (DPOD). In: Active Flow Control, vol 95. Springer, Berlin, pp 105–118
29. Schmid PJ (2010) Dynamic mode decomposition of numerical and experimental data. J Fluid Mech 656:5–28
30. Chen KK, Tu JH, Rowley CW (2012) Variants of dynamic mode decomposition: boundary condition, Koopman, and Fourier analyses. J Nonlinear Sci 22(6):887–915
31. Siegel S, Cohen K, McLaughlin T (2006) Numerical simulations of a feedback-controlled circular cylinder wake. AIAA J 44:1266–1276

32. Gallardo D, Bevilacqua R, Sahni O (2014) Data-based hybrid reduced order modeling for vortex-induced nonlinear fluid-structure interaction at low Reynolds numbers. J Fluids Struct 44:115–128
33. Ge X, Wen JT (2011) Hybrid model reduction for compressible flow controller design. In: Proceedings of the 50th IEEE conference on decision and control and European control conference, Orlando, Florida
34. Zhu Y (2002) Estimation of an N-L-N Hammerstein–Wiener model. Automatica 38:1607–1614
35. Bai EW (2002) A blind approach to the Hammerstein–Wiener model identification. Automatica 38:967–979
36. Bloemen HHJ, Van Der Boom TJJ, Verbruggen HB (2001) Model-based predictive control for Hammerstein–Wiener systems. Int J Control 74(5):482–495
37. Janczak A (2004) Identification of nonlinear systems using neural networks and polynomial models: a block-oriented approach. In: Lecture Notes in Control and Information Sciences, vol 310. Springer, Berlin
38. Murphy MJ, Dieterich S (2006) Comparative performance of linear and nonlinear neural networks to predict irregular breathing. Phys Med Biol 51(22):5903–5914